

1 Improved modeling of the Arctic halocline with a
2 sub-grid-scale brine rejection parameterization

A. T. Nguyen and D. Menemenlis and R. Kwok

3 Jet Propulsion Lab, California Institute of Technology, Pasadena, California,
4 USA

A. T. Nguyen, Jet Propulsion Lab, California Intitute of Technology, MS 300-323, 4800 Oak Grove Dr, Pasadena CA 91109-8099, USA. (An.T.Nguyen@jpl.nasa.gov)

D. Menemenlis, Jet Propulsion Lab, California Intitute of Technology, MS 300-323, 4800 Oak Grove Dr, Pasadena CA 91109-8099, USA. (Dimitris.Menemenlis@jpl.nasa.gov)

R. Kwok, Jet Propulsion Lab, California Intitute of Technology, MS 300-235, 4800 Oak Grove Dr, Pasadena CA 91109-8099, USA. (Ronald.Kwok@jpl.nasa.gov)

Abstract. The halocline in the Arctic Ocean plays an important role in regulating heat exchange at the bottom of the mixed layer and it has a direct effect on the ocean sea-ice energy balance and sea-ice mass balance. Modeling the halocline, however, remains a challenge in current state-of-the-art coupled ocean sea-ice models including those that participated in the Arctic Ocean Model Intercomparison Project. In this study, we successfully reproduce a cold halocline in the Canadian Basin by implementing a sub-grid-scale brine rejection parameterization in an ocean general circulation model. The brine rejection scheme improves the solution by redistributing surface salts rejected during sea-ice formation to their neutral buoyancy depths. The depths are based on salt-plume physics and published laboratory and numerical experiments. Compared with hydrographic data from 1993-2004, distribution of most of the rejected salt to the bottom of the mixed layer seems to yield the lowest model-data misfits. We also show that the model's mixed layer depth is sensitive to the background diffusivity ν used in the K-Profile Parameterization vertical mixing scheme. A background diffusivity of $10^{-6} m^2/s$ in combination with brine rejection scheme described herein yield the best simulation of the Arctic halocline.

1. Introduction

The upper 1000m of the Arctic Ocean features a mixed layer from the surface down to approximately 50m depth, a halocline with near freezing temperature and very high salinity gradient between approximately 50-200m depth, and an Atlantic Water layer with temperature exceeding 0.5°C below 300m [Rudels *et al.*, 2004]. Using hydrographic data from the Sea Ice Expedition (SCICEX) cruises, Steele and Boyd [1998] and Boyd *et al.* [2002] found that the halocline had retreated in the Eurasian Basin in the early 1990s and partially recovered in 1998-2000. In the Canadian Basin, however, the halocline is still a prominent feature at depth \sim 50-250m, as observed in conductivity-temperature-depth (CTD) casts from SCICEX cruises [Rudels *et al.*, 2004; Steele and Boyd, 1998] and from the Beaufort Gyre Experiment Project (BGEF) in 2003-2004 [Kemp *et al.*, 2005]. Without the halocline, heat from the Atlantic Water can get entrained into the mixed layer and melt significant amount of Arctic sea-ice [Steele and Boyd, 1998]. Thus, the halocline plays a vital role in regulating heat input into the mixed layer from below, and has a direct effect on the ocean sea-ice energy balance and sea-ice mass balance [Steele and Boyd, 1998].

Modeling a realistic halocline remains a challenge in current state-of-the-art coupled ocean sea-ice models. In the Arctic Ocean Model Intercomparison Project (AOMIP), 10 state-of-the-art Arctic Ocean and Sea-ice models were compared with each other. All 10 models failed to reproduce the halocline partly due to lack of physics in vertical mixing process and/or shelf/basin exchanges (Fig. 1, [Holloway *et al.*, 2007]). Specifically, all models produced a temperature gradient from depth \sim 50-200m, in contrast to the near-

freezing temperature observed between these depths in the Amerasian domain (Fig. 1).

A coupled ocean and sea-ice configuration of the Massachusetts Institute of Technology general circulation model (MITgcm) produces a similar temperature gradient in the Arctic. In our initial investigation we found that excessive vertical mixing (a) destroys the steep salinity gradient associated with the halocline, (b) deepens the mixed layer depth, and (c) brings heat from the Atlantic Water to near the surface to create the observed temperature gradient.

A similar problem with salinity gradient degradation was observed in ocean general circulation models in the Southern Ocean. *Duffy and Caldeira* [1997] and *Duffy et al.* [1999] showed that excessive vertical mixing destroyed the sharp pycnocline associated with the Antarctic Intermediate Water (AAIW). To address this issue, *Duffy and Caldeira* [1997] and *Duffy et al.* [1999] introduced a sub-grid salt-plume scheme to reduce grid-scale vertical mixing. *Duffy and Caldeira* [1997] justification for sub-grid parameterization is that salt-rejection occurs at $\sim 1\text{-}10\text{km}$ scale which is too small for global circulation models to resolve. In their parameterization, salt rejected from sea-ice formation was distributed uniformly down to a depth of density 0.4kg/m^3 higher than the surface density. When they turned on the salt-plume scheme, the sharp salinity gradients associated with the AAIW in the model were preserved. In addition to reproducing the AAIW, they were also able to realistically simulated the North Atlantic Deep Water and the Antarctic Circumpolar Current. In this study, we implement a parameterization similar to *Duffy et al.* [1999] in a regional configuration of the MITgcm to improve the vertical salinity structure in the Arctic and to reproduce the halocline. Primary differences between our scheme and that of *Duffy et al.* [1999] include the criteria for determining the depth to

which the rejected brine is mixed, and a salt vertical distribution function. Available conductivity-temperature-depth (CTD) data are used to assess the model performance. In addition, we also investigate the effect of background diffusivity on vertical mixing.

The outline of the paper is as follows. Section 2 summarizes the physics of brine mixing based on previous laboratory experiments and numerical studies of brine rejection during sea-ice formation. The parameterization of brine rejection in our model is described in detail in Section 3. Sections 4 and 5 describe the CTD data and model configuration and numerical experiments. In Section 6 we present and discuss results of the sensitivity experiments to examine the modeled halocline of the Arctic Ocean. A summary of our findings and final remarks are in Section 7.

2. Salt-plume physics

2.1. Theory and previous laboratory experiment results

Seasonal sea-ice can retain up to 30% of the sea-water salinity in brine pockets and melt frozen ponds and has salinity of about 10psu [Nakawo and Sinha, 1981]. The remaining salt is rejected as brine into the ocean. Scaling analyses and laboratory experiments by Morton et al. [1956]; Scorer [1957]; Helfrich [1994]; Bush and Woods [1999] show that when salt is introduced into a density stratified fluid, the depth to which the salt penetrates and the horizontal extent of the salt distribution are controlled mainly by the initial buoyancy, the fluid stratification strength, and the fluid rotation rate. Assume that a point-source plume is released from rest with a horizontal scale b and vertical extent z as shown in Fig. 2, and let f be the Coriolis frequency, V_o the initial volume of the plume, ρ_o and ρ_a the initial salt-plume and ambient densities, respectively, the initial salt-plume buoyancy F_o in unit of m^4/s^2 is

$$F_o = V_o \cdot g \frac{\rho_o - \rho_a}{\rho_a} \quad (1)$$

where g is the gravitational acceleration. The fluid density stratification is expressed, in terms of N , the *Brunt – Väisälä* frequency, as follows,

$$N^2 = -\frac{g}{\rho} \frac{d\rho}{dz}, \quad (2)$$

In the case $N/f \gg 1$ and where rotation is unimportant, *Morton et al.* [1956] showed that the rejected salt penetrates to a neutral-buoyancy depth z_M and has a horizontal spread radius b_M described by:

$$z_M \approx k_1 [F_o N^{-2}]^{1/4} \quad (3)$$

$$b_M \approx k_2 z_M \quad (4)$$

Values of k_1 and k_2 are 2.66 and 0.25 based on scaling analyses [*Scorer*, 1957]. Laboratory experiments by *Helfrich* [1994] show that the salt-plume overshoots z_M slightly, but stabilizes at this depth and begins to spread horizontally as an axisymmetric intrusion until time $t \sim f^{-1}$ when rotation becomes significant. The plume then breaks into small anticyclonic eddies and gets entrained into the surroundings [*Helfrich*, 1994].

In the case where stratification $d\rho/dz$ is weak and rotation dominates, $N/f \ll 1$, the salt lateral growth is constrained to columns of radius b_R at an approximate depth z_R with time-scale $t \sim f^{-1}$ [*Scorer*, 1957] such that,

$$z_R \approx k_3 [F_o f^{-2}]^{1/4} \quad (5)$$

$$b_R \approx k_4 z_R \quad (6)$$

Scaling analyses and experimental values for $[k_3, k_4]$ are $[3.6, 0.25]$ and $[4.94, 0.21]$, respectively [Scorer, 1957; Helfrich, 1994]. The salt column then continues to penetrate as a Taylor column of radius b_R until it reaches approximately the neutral buoyancy depth z_M where it breaks up into anticyclonic and cyclonic pairs of eddies due to geostrophic adjustment [Helfrich, 1994]. The transition between stratification-controlled and rotation-controlled regimes occurs at approximately $N/f \sim 0.6$ and is independent of the initial plume buoyancy F_o [Helfrich, 1994].

When the plume source is 2-D and continuous for some finite time t_s , as is the case during lead openings and sea-ice freezing [Morison et al., 1992], the physics of the plume penetration remains similar to its 1-D counterpart, with some modifications [Bush and Woods, 1999]. In this case, the important parameters are the Coriolis frequency f , Brunt – Väisälä frequency N , the length scale of the line source L , and the plume buoyancy flux per unit length B_o . B_o depends on the volume flux per unit length $Q_o(m^2/s)$ as follows,

$$B_o = Q_o \cdot g \frac{\rho_o - \rho_a}{\rho_a} \quad (7)$$

B_o has unit $[m^3/s^3]$. Again, the two cases to consider are when stratification dominates ($N/f \gg 1$) and when rotation dominates ($N/f \ll 1$). For most oceanic applications, the first case, $N/f \gg 1$, is most relevant and will be covered here [Bush and Woods, 1999]. The neutral buoyancy depth z_M to which the 2-D salt-plume penetrates is derived from laboratory experiments by Bush and Woods [1999] as follows,

$$z_M \approx (3.0 \pm 1.0) \frac{B_o^{1/3}}{N} \quad (8)$$

After reaching z_M , the 2-D salt-plume spreads horizontally until time $t \sim f^{-1}$ when it breaks up into multiple anticyclonic vortexes with characteristic radii that scale with B_o and t_s .

2.2. Previous numerical modelings and field studies

The 2-D experiment in Section 2.1 provides insights into how rejected salt mixes under leads. Winter leads are openings due to divergence of sea-ice, and have typical length-scales of 50-1000m in width and 1-50km in length [Morison *et al.*, 1992]. The large heat exchange between the relatively warm water and very cold air $-15^\circ C$ to $-20^\circ C$ results in rapid sea-ice formation and brine rejection. Data from the 1974 Arctic Ice Dynamics Joint Experiment [Smith, 1974; Morison, 1978], the 1976 Arctic Mixed Layer Experiment [Morison *et al.*, 1992], and the 1992 Lead Experiments [Muench *et al.*, 1995; Morison and McPhee, 1998] show that when the ice velocity is less than $\sim 0.10m/s$, the following processes as shown in Fig 3 are consistently observed. Salt-plumes first form at the edges of the lead, then sink to the bottom of the mixed layer and spread out horizontally away from the lead axis (see heavy vertical arrows in Fig 3). At the surface, returning flows advect freshwater horizontally toward the lead center (short gray horizontal arrows in Fig 3). When ice velocity is large, turbulent forces dominate and distribute the brine throughout the mixed layer.

The lead-induced salt-plume convections are well reproduced in numerical models [Kozo, 1983; Smith IV and Morison, 1993, 1998; Smith IV *et al.*, 2002]. Kozo [1983]; Smith IV

and Morison [1998] modeled brine rejection in a 2-D domain of size $\sim 2500m$ wide by
 100m deep with a lead 750m wide at the center (Fig. 3). A halocline of gradient $d\rho/dz \sim$
 $0.005kg/m^3/m$ is placed at 40m depth. As sea-ice begins to form at the edges of the lead,
 plumes of sizes comparable to the lead's width sink to the bottom of the mixed layer, then
 spread out horizontally away from the lead center [Smith IV and Morison, 1998]. The
 vertical salt flux they observed of $\sim 5 \cdot 10^{-5}kg/m^2/s$ and salinity disturbances $\Delta S \sim 0.01-$
 0.02 are consistent with observations. In one experiment, salt-plumes weakly penetrate
 the halocline. However, this is only the case when the buoyancy force is very high and
 there is no relative ice-ocean velocity at the surface. Rotation does not play an important
 role in salt-plume convection in the Arctic because the halocline is at too shallow depth
 ($\sim 40m$) compared to the depth required for rotational effect ($\sim 3000-4500m$, [Smith IV
et al., 2002]).

In summary, both numerical models and field observations show consistent patterns of
 buoyancy convection associated with brine rejection beneath leads. The plume sinks to
 the bottom of the mixed layer, but can not penetrate the halocline. Instead, it spreads
 horizontally along the top of the halocline, and reduces the depth of the mixed layer
 [Morison *et al.*, 1992]. The horizontal extent of salt-plume convection is of the order $\sim 3 \times$
 the width of the lead [Smith IV and Morison, 1998]. Given that typical lead widths are
 $\sim 50-1000m$, buoyancy convection will have typical horizontal extent of $\sim 100-3000m$. Most
 global ocean models cannot resolve convection at this horizontal length scale [Duffy and
 Caldeira, 1997]. As a result, the rejected salt at the surface is spread across the entire grid
 which in turn causes instability and large-scale convection in the mixed layer. Large-scale
 convection in turn deepens the mixed layer in contrast to observations, laboratory and

numerical experiment results [Morison *et al.*, 1992; Helfrich, 1994; Smith IV and Morison, 1998; Duffy and Caldeira, 1997]. In the next section, we discuss the implementation of a sub-grid salt rejection scheme to address this large grid-scale convection problem.

3. Salt-plume parameterization in our MITgcm configuration

3.1. Brine rejection treatment

As mentioned earlier, Duffy and Caldeira [1997] and Duffy *et al.* [1999] introduced sub-grid brine rejection parameterization to reproduce the sharp salinity gradients associated with the AAIW in the Southern Ocean, and their success motivated us to implement a similar scheme for the Arctic Ocean. In our model, sea-ice retains 30% of the top layer's salinity during freezing. The remaining salt (70%) is rejected back to the ocean. Duffy *et al.* [1999] distributed the salt uniformly from the surface down to a depth with density $0.4kg/m^3$ greater than the surface density ρ_{surf} . The value of $\Delta\rho = 0.4kg/m^3$ was chosen to best fit their model results to observations in the Southern Ocean. In place of the uniform distribution, here we introduce a simple depth dependent distribution function of salt $s(z)$ and the corresponding cumulative function $S(z)$ as follows,

$$s(z) = \begin{cases} Az^n & \text{if } |z| \leq |D_{sp}|; \\ 0 & \text{if } |z| > |D_{sp}| \end{cases} \quad (9)$$

$$S(z) = \int_0^{D_{sp}} s(z) dz \quad (10)$$

n and D_{sp} are the distribution power and salt-plume depth, respectively, and are adjustable parameters. $S(z)$ is the cumulative salt as a function of depth z , with $S(z = D_{sp})$ constrained to equal to the total amount of rejected salt S_o . The con-

stant $A = (n + 1)/D_{sp}^{(n+1)}$ is determined using the above constraint of $S(z = D_{sp}) = S_o$. Fig. 4 shows the distribution functions for $n = [0 - 7]$. *Duffy et al.* [1999] used a criterion $\Delta\rho = \rho(z) - \rho_{surf} = 0.4kg/m^3$ to determine D_{sp} , then set $n = 0$ which yielded $s(z) = A = 1/D_{sp}$ for a uniform distribution (Fig. 4, dark blue curve).

Based on laboratory and numerical experiment results discussed in Section 2, most of the salt reaches the bottom of the mixed layer depth instead of mixing down uniformly. This suggests a value of n larger than 1. To determine D_{sp} , we locate the depth immediately below the mixed layer and above the halocline. With the high salinity gradient in the halocline, we use a $d\rho/dz$ instead of a $\Delta\rho$ criterion to determine D_{sp} . In the mixed layer, density is relatively uniform with $d\rho/dz \approx 0$. In the halocline, typical density gradients are of the order $d\rho/dz \approx [0.01, 0.03]kg/m^3/m$. Our initial investigation showed that a $d\rho/dz \approx 0.012kg/m^3/m$ with $n \approx 5$ yielded the lowest misfits between model results and CTD data. Fig. 5 shows maps of the oceanic boundary layer (mixing layer) as calculated from the K-Profile Parameterization (KPP) vertical mixing scheme [*Large et al.*, 1994] and the corresponding salt-plume depth D_{sp} using the criterion $d\rho/dz \approx 0.012kg/m^3/m$. High values of n yield distribution functions $s(z)$ which are consistent with laboratory experiments showing most of the salt reaching the neutral buoyancy depth (Fig 4). Model results for $n > 5$ are not significantly different from those with $n = 5$. In the sensitivity experiments discussed in this paper, we use $n = 5$.

3.2. Brine rejection with KPP vertical mixing

Our configuration of the MITgcm uses the KPP from *Large et al.* [1994] to calculate vertical mixing in the Oceanic Boundary Layer (OBL) and in the deep ocean. The OBL depth is determined using a local bulk Richardson number Ri_b and a critical bulk Richardson

number Ri_{cr} criterion. Ri_b is roughly defined as $Ri_b(z) \sim z\Delta B/\Delta V^2$, where z is depth, ΔB is the differential buoyancy between near surface and bottom of mixed layer, and ΔV^2 the differential shear (Fig. 6). An increase in ΔB implies a sharper density gradient with depth, hence a steeper $Ri_b(z)$ (compare curve 2 to 1 in Fig. 6). On the other hand, when there is increasing differential shear ΔV^2 , $Ri_b(z)$ will be shallower (curve 3 in Fig. 6). For a given Ri_{cr} (dashed heavy black line in Fig. 6), the location where $Ri_b(z)$ crosses Ri_{cr} defines approximately the depth of the OBL in the KPP scheme. Thus, for an increase in ΔB and ΔV , the mixing layer is shallower ($z_{\Delta B}$ in Fig. 6) and deeper ($z_{\Delta V}$ in Fig. 6), respectively.

When the salt-plume scheme is turned on, rejected salt is removed from the surface and added to the bottom of the mixed layer. As a consequence, salinity and density gradients and ΔB are higher than in the case when salt-plume is turned off. This results in a shallower OBL depth when the salt-plume scheme is used (case 2 in Fig. 6).

4. Data

Observational data used to assess the proposed sub-grid-scale parameterization are conductivity-temperature-depth (CTD) measurements from the Scientific Ice Expeditions (SCICEX, [Langseth et al., 1993; Moustafa et al., 1998; Hopkins et al., 1998; Boyd et al., 1998; Edwards et al., 1999; Rothrock et al., 1999]) and the Beaufort Gyre Exploration Project (BGEP, [Kemp et al., 2005]). The data span the years 1993-2000 for SCICEX and 2003-2004 for BGEP data. Single measurement accuracies range from ± 0.001 to $\pm 0.005^\circ C$ for temperature and approximately ± 0.005 for derived salinity (<http://www.seabird.com>, <http://falmouth.com>). Data are downloaded from <http://www.ldeo.columbia.edu/>,

<http://nsidc.org>, and <http://www.whoi.edu/beaufortgyre/>. Fig. 7 shows the spatial distribution of the data in the four basins in the Arctic and in the Chukchi Cap area.

5. Numerical sensitivity experiments

To reduce computational cost, we use a regional Arctic Ocean configuration of the MIT-gcm global grid to reduce the computational cost. The model has horizontal resolution of $\sim 18km$ and 50 vertical levels. Surface forcings are from ERA-40 and ECMWF. Boundary conditions are monthly and are taken from the latest global optimized solution [Zhang *et al.*, 2008]. Initial conditions are from the World Ocean Atlas 2005 [Antonov *et al.*, 2006; Locarnini *et al.*, 2006] starting in January 1992. Initial sea-ice condition is from Zhang and Rothrock [2003]. The model is allowed to run until the end of October 2006.

A set of nine experiments as shown in Table 1 is performed. The baseline, **A0**, is the first optimized Arctic MITgcm solution as reported in Nguyen *et al.* [2008]. The rest of the experiments use parameters from **A0**, but with changing background diffusivity ν and with the salt-plume scheme turning on or off. Experiments **A1** and **A2** are background diffusivity sensitivity experiments. Zhang and Steele [2007] showed that their regional model with a KPP background diffusivity $\nu \sim 10^{-6}m^2/s$ (ν_s^w in Large *et al.* [1994]) in the Arctic reproduced the most realistic Atlantic Water layer and circulation. Compared to observations, Zhang and Steele [2007] showed that further decrease of ν in combination with KPP being turned off resulted in unrealistic build up of fresh water at the surface and build up of heat in the halocline as well as too shallow mixed-layer depth. Here we investigate the sensitivity of the upper ocean in the Arctic to both ν and salt rejection.

6. Results and Discussion

Fig. 7 shows the geographic locations of the Nansen (purple, 1), Amundsen (dark blue, 2), Makarov (light blue, 3), Canadian Basins (red, 4) and Chukchi Cap (green, 5), as well as CTD data distribution and typical vertical salinity/temperature profiles within each region based on observations. The halocline is most distinctive in the Canadian Basin and Chukchi Cap, extending down to depth $> 250m$ (Fig. 7b, curves 4-5), and is progressively shallower in the Makarov (curve 3) and Amundsen Basins (curve 2). In the Nansen Basin, the halocline is entirely missing (low salinity gradient in curve 1), and the mixed layer extends down all the way to the top of the Atlantic Water [Rudels *et al.*, 2004]. The Atlantic Water, roughly defined as water with temperature $> 0^{\circ}C$, transitions from warmer and shallower in the Nansen Basin to cooler and deeper in the Canadian Basin (curves 1-4 for temperature in Fig. 7b).

As mentioned in Section 1, AOMIP and our models fail to reproduce the large salinity gradient and near freezing temperature observed in the halocline (Fig. 1). Here, we assess the effectiveness of the sub-grid brine rejection scheme on vertical mixing and on the reproduction of the halocline in the individual basins and in the Chukchi Cap area. For the Canadian, Makarov, and Amundsen Basins and for the Chukchi Cap, a minimum of ten CTD profiles is used each year to obtain model-data misfits and statistics. In the Nansen Basin where data are sparse, a minimum of five CTD profiles is used for assessment calculations. To measure the sensitivity experiment's improvement relative to the baseline, we first compute the sum of squares of residuals (SSQ), then calculate the percentage of improvement I as follows,

$$I = \frac{(SSQ_{baseline} - SSQ_{sensitivity})}{SSQ_{baseline}} \times 100 \quad (11)$$

I is positive when the sensitivity experiment fits CTD observations better than the baseline, i.e., $SSQ_{sensitivity} < SSQ_{baseline}$, and negative when the fit is worse, i.e., $SSQ_{sensitivity} > SSQ_{baseline}$. **A0** is the baseline and **A{1-2}** and **A{0-2}_sp{1-2}** are sensitivity experiments. Outliers in the data are removed to ensure I is not dominated by a few large residual points.

6.1. Canadian Basin

Results for all the years when CTD data are available, 1993-2004, are summarized in Table 2, and vertical profiles and Temperature/Salinity (T/S) diagram for 2003 are shown in Fig. 8. In the first seven years (1992-1999), experiments with reduced background diffusivity (**A1**, **A2**) give similar improvements I as those with salt-plume schemes (**A0_sp1**, **A0_sp2**, Table 2). For example, in 1995, $I = [24\%, 27\%]$ for **A1**, **A2** and $I = [38\%, 28\%]$ for **A0_sp1**, **A0_sp2** (Table 2, columns 4-6). However, a decreased ν preconditioned the ocean stratification in such a way as to inhibit the episodic vertical mixing in the mixed layer. As a result, the top layers in the model became highly stratified with the mixed layer depth approaching the surface, consistent with results reported in *Zhang and Steele* [2007]. The effect of small ν on mixed layer depth becomes more apparent in the later years of the simulation (\sim 2000-2004), when I for experiments **A{1-2}** become progressively smaller than those with the salt-plume scheme (Table 2, columns 4-6).

The salt-plume scheme affects vertical mixing in two ways. When there is an excess of rejected salt, the scheme mixes the salt down at sub-grid level, thus decreases the likelihood

of large grid-scale vertical mixing and prevents the deepening of the mixed layer (compare Fig. 5b and Fig. 5c). The short time-scale effect of the scheme on the mixed layer depth is similar to that of reduced vertical background diffusivity ν . However, when the mixed layer depth becomes too shallow with small ν values, the salt-plume scheme enables vertical mixing of heat and salt and prevents the top layers from being overheated and becoming too fresh. This effect is observed in the later years (~ 2000 -2004) when the salt-plume experiments **A2_sp1** and **A2_sp2** yield the largest I values (Fig. 8, Table 2, columns 5-6). In the Canadian Basin, a combination of background diffusivity $\nu \sim 10^{-6} m^2/s$ and deeper salt-plume depth D_{sp} which corresponds to $d\rho/dz \approx 0.018 kg/m^3/m$ reduces data-model misfits to less than half the baseline **A0**'s values (i.e., $\sim 100\%$ improvement) for both temperature and salinity (Table 2). The misfit in the lower halocline from Atlantic Water source ("e" in Fig. 8) will be discussed later.

6.2. Chukchi Cap

Vertical T/S profiles in the Chukchi Cap are similar to those in the Canadian Basin. CTD data are limited to only 4 years in the Chukchi Cap area (Fig. 9, Table 2, columns 7-10), but yield results with consistent patterns of reduced misfits in lower background diffusivity experiments (**A{1-2}**) during the early years (1993-1998), followed by reduced misfits in salt-plume experiments in the later years (1999-2003). Both the mixed layer depth and halocline are shallower in experiments **A1**, **A2** and deeper in **A1_sp2**, **A2_sp2** compared to the baseline experiment **A0** (Fig. 9, upper panel). With salt-plume scheme turned on, the warm temperature signature near depth 50-100m is sustained for the 14-year duration of the experiment. In addition, the temperature associated with the Bering Strait Winter Water ("c" in Fig. 8, 9) is better reproduced. Large misfits at depth below

150m are related to issues with the Atlantic Water outside the Arctic Ocean and will be discussed later in detail.

6.3. Makarov and Amundsen Basins

The biggest improvements in the Makarov and Amundsen Basins are in salinity gradient within the halocline, and temperature in the Atlantic Water layer (Fig. 10). At the surface, temperature is warmer than observed in both basins. The baseline experiment **A0** has temperature closest to the observations between depths 0-100m (dark blue curve in Fig. 10, upper panels), but does not have the correct physics: Based on the low salinity gradients within these depths in **A0**, the approximate constant temperature is reflective of a mixed layer depth of $\sim 100m$, which is not observed in the salinity data (compare S profiles between dark blue and black dashed curves in Fig 10). At close to freezing temperature, density is a strong function of salinity and is practically independent of temperature (see contour lines in T/S diagram in Fig. 10). As a result, decreased misfits in salinity have more physical significance than in temperature. With the salt-plume scheme turned on, rejected salt at the surface is redistributed to greater depth, resulting in higher salinity gradients and better fit to the observations (Fig. 10, compare S profiles of **A{1-2}_sp{1-2}** to those of **A{1-2}** and to data). The pattern of improved fit in the early years for lower background diffusivity experiments and later years for salt-plume experiments also holds true in both basins (Table 2, columns 11-18).

6.4. Nansen Basin

In the Nansen Basin, the halocline is almost entirely missing and the mixed layer extends down to near the top of the Atlantic Water layer (Fig. 7b curve 1, [Rudels et al., 2004]).

Data in this basin are sparse, with less than 10 profiles per year (Table 2, columns 19-22). Salt-plume experiments **A{0-2}-pl{1-2}** fit salinity and temperature observations reasonably in the Atlantic Water layer (Fig. 11). However, all nine experiments fail to reproduce the deep mixed layer in the top 150m. At the surface, salt-plume experiments produce more consistent salinity values (~ 33) compared to observations (see salinity profiles in upper panel of Fig. 11). The good fit in temperature at depths $\sim 0-50m$ between the baseline experiment **A0** and data is again questionable because **A0**'s surface salinity is fresher by ~ 2.5 and **A0**'s salinity gradient in the top 150m is too high compared to observations (Fig. 11). With small background diffusivities (**A1**, **A2**), surface salinity remains too fresh by $\sim 1.5-2.0$ (Fig. 11, upper panel).

One reason for the large misfits in the Nansen Basin is the model's inability to reproduce the Atlantic Water in the Greenland Sea [Nguyen *et al.*, 2008]. In our baseline solution **A0**, the Atlantic Water is deeper, thicker, and significantly colder than observed in the Greenland Sea. As a consequence, the water flowing into the Arctic Ocean through Fram Strait does not have the correct properties, and results in lower volume and heat transports across Fram Strait compared with observations [Nguyen *et al.*, 2008]. After entering the Arctic Ocean through Fram Strait and the St. Anna Trough (see Fig. 2 for locations), Atlantic Water mixes with surface melt water and flows along the Siberian side into the Makarov and Canadian Basins and the Chukchi Cap area [Rudels *et al.*, 2004]. Upon reaching the Canadian Basin, mixed water from Atlantic source, which is more dense than from Pacific source, submerges beneath to form the lower halocline ("e" in Fig. 8, [Steele and Boyd, 1998]). Due to problems with simulated inflow Atlantic Water in our model, the lower halocline in the Canadian Basin and Chukchi Cap area can not be

realistically reproduced in the experiments presented here (Fig. 8, 9, vertical bars with label "e").

6.5. Salt plume parametrization and heat budget

One concern we have is the heat build-up in the Nansen and Amundsen Basins when the salt-plume scheme is used (T profiles in Fig. 10 and 11). To understand the origin of this build-up, we calculate heat budgets for the Amerasian (Canadian, Makarov, Chukchi Cap) and Eurasian (Amundsen and Nansen) Basins and the Greenland Sea (Fig. 12). The heat build-up in the Eurasian Basin over the 16-year model run is approximately $2 \times 10^{19} \text{J/decade}$ and is entirely explained for by the warming in the Greenland Sea (Fig 12). The warming in the Amerasian Basin is less than half of that in the Eurasian Basin. The salt-plume scheme, by design, reduces large-scale vertical heat diffusion. As a result, the extra heat transported from the Greenland Sea through Fram Strait into the Arctic Ocean remains largely in the Nansen Basin and causes the basin to heat up. The drift in heat content obtained in our model for both Amerasian and Eurasian Basins are on the lower end when compared to drifts in AOMIP models [*Holloway et al.*, 2007]. Sources for these drifts include model resolution and initial conditions, and a full investigation of the heat drifts is beyond the scope of this study.

7. Summary and Outlook

Sub-grid vertical mixing of rejected salt during sea-ice formation is implemented in a regional configuration of the MITgcm coupled ocean sea-ice model to successfully reproduce the halocline in the Arctic ocean. When a KPP background diffusivity value $\nu \approx 10^{-5} \text{m}^2/\text{s}$ is used without the salt-plume scheme, grid-scale convection is more likely

to occur and mixed layer depths exceeding 70m in the Canadian Basin are seen in the solutions. Such deep mixed layers destroy the halocline and produce unrealistic temperature gradients seen in all basins for our baseline experiment **A0** and in the AOMIP participating models' outputs. Decreasing background diffusivity initially improved the model fit to data. However, over the 14-yr model run, small background diffusivity pre-conditions the ocean such that vertical mixing is inhibited and results in the top 50m becoming unrealistically too warm and fresh. A KPP background diffusivity value $\nu = 10^{-6} m^2/s$ works best for our model and is consistent with the published value in *Zhang and Steele [2007]*.

Turning on the salt-plume scheme reduces the unrealistic large grid-scale vertical mixing, which is an artifact of the model's limited resolution. The scheme takes salt at the surface and distributes it down to the depth of neutral buoyancy and results in a stabilized halocline in the Canadian Basin and Chukchi Cap at the end of the 14-year model run. A salt-plume scheme with parameters $d\rho/dz = 0.018 kg/m^3/m$ and $n = 5$, which correspond to distributing most of the rejected salt to the bottom of the mixed layer, yield the lowest model-data misfits when compared to hydrographic observations in Amundsen, Makarov, and Canadian Basins and in the Chukchi Cap. One exception is in the Nansen Basin where the our model does not reproduce the observed deep mixed layer. A reason for this is the heat build-up in the the Greenland Sea which we plan to address in future work. Additional possibilities for the large misfits in the Nansen Basin include mis-representation of the Atlantic Water and unmodeled sub-grid eddy processes due to the model resolution limitation.

The halocline plays a vital role in regulating heat transport into the mixed layer and in the energy exchange at the ocean sea-ice interface. Yet modeling a halocline remains a challenge in current state-of-the-art coupled ocean sea-ice models due to missing physics and resolution limitation. This study presents an important contribution to numerical modeling of the Arctic upper ocean. Specifically, we address the problem of the missing halocline, and show that brine rejection at sub-grid scale can be used to reproduce and maintain a realistic halocline in our regional configuration of the MITgcm. In addition, we also show the importance of the background diffusivity in the KPP vertical mixing scheme to the mixed layer. Coupled ocean sea-ice models with realistic halocline and mixed layer will improve estimates of the ocean sea-ice energy exchange at the surface and estimates sea-ice mass balance in the Arctic Ocean.

Acknowledgments. This work is funded by the Estimating the Circulation and Climate of the Ocean, Phase 2 (ECCO2) project, a contribution to the NASA Modeling Analysis and Prediction (MAP) program. We gratefully acknowledge computational resources and support from the NASA Advanced Supercomputing (NAS) Division and from the JPL Supercomputing and Visualization Facility (SVF). We would like to thank two anonymous reviewers for helpful comments and discussions.

References

Antonov, J., R. Locarnini, T. Boyer, A. Mishonov, and H. Garcia (2006), Volume 2: Salinity, in *World Ocean Atlas 2005*, edited by S. Levitus, p. 182pp, NOAA Atlas NESDIS 62, U.S. Government Printing Office, Washington D.C.

- Boyd, T., M. Moustafa, and M. Steele (1998), Submarine-based hydrographic observations of the Arctic Ocean, *Oregon State University*, ref. 97-3 Data Report 165.
- Boyd, T., M. Steele, R. Muench, and J. Gunn (2002), Partial recovery of the Arctic Ocean halocline, *Geophys. Res. Lett.*, *29*(14), 1657, doi:10.1029/2001GL014047.
- Bush, J., and A. Woods (1999), Vortex generation by line plumes in a rotating stratified fluid, *J. Fluid Mech.*, *388*, 289–313.
- Duffy, P., and K. Caldeira (1997), Sensitivity of simulated salinity in a three-dimensional ocean model to upper ocean transport of salt from sea-ice formation, *Geophys. Res. Lett.*, *24*(11), 1323–1326.
- Duffy, P., M. Eby, and A. Weaver (1999), Effects of sinking of salt rejected during formation of sea ice on results of an ocean-atmosphere-sea ice climate model, *Geophys. Res. Lett.*, *26*(12), 1739–1742.
- Edwards, M., B. Coakley, D. Chayes, S. Okkonen, M. Rognstad, D. Stockwell, and T. Whitledge (1999), Arctic basin insights 1: New data for the Amerasian Basin from SCICEX-99, *Eos Trans. AGU*, *80*(46), Fall Meet. Suppl., Abstract T31F-08.
- Helfrich, K. (1994), Thermals with background rotation and stratification, *J. Fluid Mech.*, *259*, 265–280.
- Holloway, G., F. Dupont, E. Golubeva, S. Hakkinen, E. Hunke, M. Jin, M. Karcher, F. Kauker, M. Maltrud, M. M. Maqueda, W. Maslowski, G. Platov, D. Stark, M. Steele, T. Suzuki, J. Wang, and J. Zhang (2007), Water properties and circulation in Arctic Ocean models, *J. Geophys. Res.*, *112*(C04S03), doi:10.1029/2006JC003642.
- Hopkins, T., M. Moustafa, C. Kinder, and M. Cook (1998), SCICEX-96 hydrographic data report USS POGY SSN 647 polar cruise 27 August - 12 November 1996, *MEAS/NCSU*

Technical Report 98-1.

Kemp, J., K. Newhall, W. Ostrom, R. Krishfield, and A. Proshutinsky (2005), The Beaufort Gyre Observing System 2004: Mooring recovery and deployment operations in pack ice, *Tech. Rep. WHOI-2005-5*, Woods Hole Oceanographic Institute, WHOI Technical Report.

Kozo, T. (1983), Initial model results for Arctic mixed layer circulation under a refreezing lead, *J. Geophys. Res.*, *88*(C5), 2926–2934.

Langseth, M., T. Delaca, G. Newton, B. Coakley, R. Colony, J. Gossett, C. May, P. McRoy, J. Morison, WillamSmethie, D. Steele, and W. Tucker (1993), SCICEX-93: Arctic cruise of the US navy nuclear powered submarine USS PARGO, *MTS Journal*, *27*, 4–12.

Large, W., J. McWilliams, and S. Doney (1994), Ocean vertical mixing: a review and a model with a nonlocal boundary layer parameterization, *Rev. Geophys.*, *32*(4), 363–403.

Locarnini, R. A., A. V. Mishonov, J. I. Antonov, T. P. Boyer, and H. E. Garcia (2006), Volume 1: Temperature, in *World Ocean Atlas 2005*, edited by S. Levitus, p. 182pp, NOAA Atlas NESDIS 62, U.S. Government Printing Office, Washington D.C.

Morison, J. (1978), The Arctic profiling system, *Proc. of a working Working Conference on Current Measurements, Jan 11-13*, pp. 313–318.

Morison, J., and M. McPhee (1998), Lead convection measured with an autonomous underwater vehicle, *J. Geophys. Res.*, *103*(C2), 3257–3281.

Morison, J., M. McPhee, T. Curtin, and C. Paulson (1992), The oceanography of winter leads, *J. Geophys. Res.*, *97*(C7), 11,199–11,218.

Morton, B., S. G. Taylor, and J. Turner (1956), Turbulent gravitational convection from maintained and instantaneous sources, *Proc. Roy. Soc. London Series A, Math. Phys.*

454 *Sci.*, *234*, 1–23.

455 Moustafa, M., P. Mikhalevsky, M. Steele, and T. Boyd (1998), Upper Arctic Ocean hy-
456 drography observed during SCICEX-95, *J. Marine Res.*

457 Muench, R., , D. S. IV, and C. Paulson (1995), Convection beneath freezing leads: New
458 observations compared with numerical model results, *J. Geophys. Res.*, *100*(C3), 4681–
459 4692.

460 Nakawo, M., and N. Sinha (1981), Growth rate and salinity profile of first-year sea ice in
461 the high Arctic, *J. Glaciol.*, *27*(96), 315–330.

462 Nguyen, A. T., R. Kwok, and D. Menemenlis (2008), Assessment of the ECCO2 coupled
463 ocean and sea ice solution in the Arctic, 2008 Ocean Sciences Meeting, Orlando, FL,
464 Session 036.

465 Rothrock, D., W. Maslowski, D. Chayes, G. Flato, and J. Grebmeier (1999), Arctic Ocean
466 science from submarines. a report based on the SCICEX 2000 workshop, *Washing-*
467 *ton Univ Seattle Applied Physics Lab*, defense Technical Information Center OAI-PMH
468 Repository (United States).

469 Rudels, B., E. Jones, U. Schauer, and P. Eriksson (2004), Atlantic sources of the Arctic
470 Ocean surface and halocline waters, *Polar Research*, *23*(2), 181–208.

471 Scorer, R. (1957), Experiments on convection of isolated masses of buoyant fluid, *J. Fluid*
472 *Mech.*, *2*(06), 583–94.

473 Smith, J. (1974), Oceanographic investigations during the AIDJEX lead experiment, *AID-*
474 *JEX Bull.*, *27*, 125–133.

475 Smith IV, D., and J. Morison (1993), A numerical study of haline convection beneath
476 leads in sea ice, *J. Geophys. Res.*, *98*(C6), 10,069–10,083.

- 477 Smith IV, D., and J. Morison (1998), Nonhydrostatic haline convection under leads in sea
478 ice, *J. Geophys. Res.*, *103*(C2), 3233–3247.
- 479 Smith IV, D., J. Lavelle, and H. Fernando (2002), Arctic Ocean mixed-layer eddy gener-
480 ation under leads in sea ice, *J. Geophys. Res.*, *107*, 195–196.
- 481 Steele, M., and T. Boyd (1998), Retreat of the cold halocline layer in the Arctic Ocean,
482 *J. Geophys. Res.*, *103*(C5), 10,419–10,435.
- 483 Turner, J. (1969), Buoyant plumes and thermals, *Annu. Rev. Fluid Mech.*, *1*, 29–44.
- 484 Zhang, H., D. Menemenlis, T. Lee, M. Schodlok, D. Volkov, and V. Zlotnicki (2008),
485 Assessment of the ECCO2 high resolution global-ocean and sea-ice synthesis using the
486 CLIVAR/GODAE global synthesis and observations panel metrics, 2008 Ocean Sciences
487 Meeting, Orlando, FL, Session 036.
- 488 Zhang, J., and D. Rothrock (2003), Modeling global sea ice with a thickness and enthalpy
489 distribution model in generalized curvilinear coordinates, *Mon. Wea. Rev.*, *131*(5), 681–
490 697.
- 491 Zhang, J., and M. Steele (2007), Effect of vertical mixing on the Atlantic Water layer circu-
492 lation in the Arctic Ocean, *J. Geophys. Res.*, *112*(C04S04), doi:10.1029/2006JC003732.

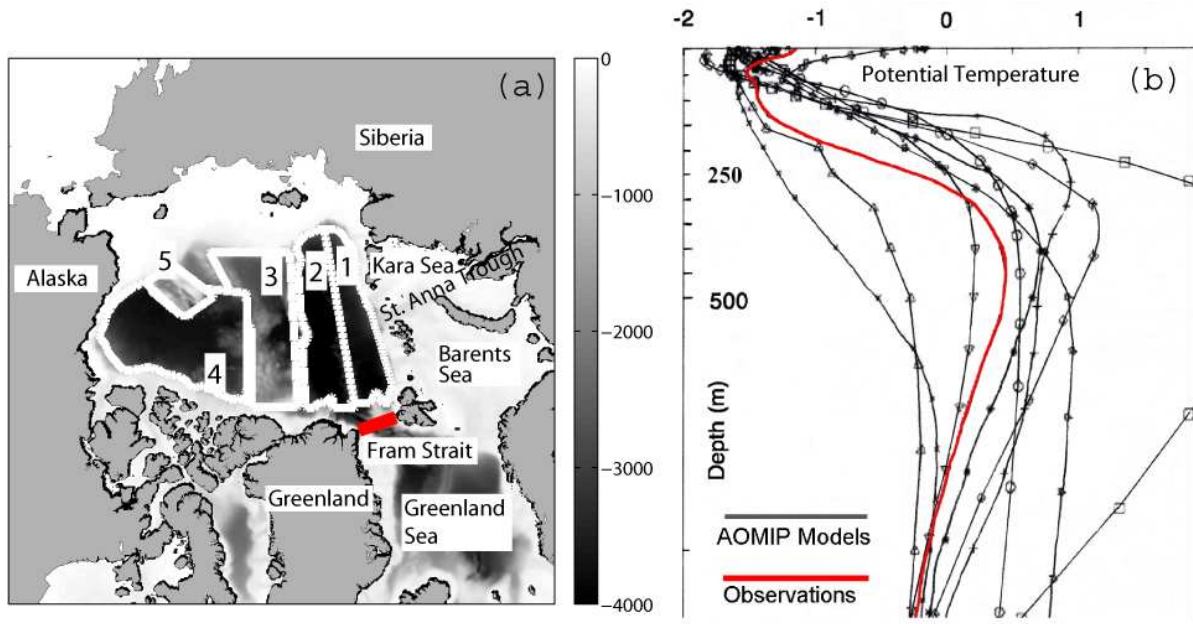


Figure 1. (a) Map of the Arctic Ocean showing the Nansen Basin (1), Amundsen Basin (2), Makarov Basin (3), Canadian Basin (4), and Chukchi Cap (5). (b) AOMIP vertical temperature profiles in the Amerasian domain (black curves) compared to observation (red curve). Amerasian domain includes the Canadian and Makarov Basins and the Chukchi Cap. The halocline is the region between depth 50m to 200m where temperature is near freezing and salinity gradient is high. In contrast to observation, AOMIP results show a temperature gradient from depth 250m to the surface. Fig. 1b is from *Holloway et al.* [2007].

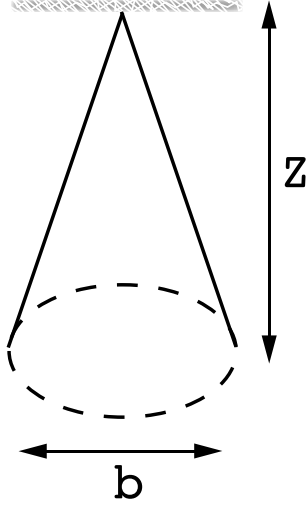


Figure 2. Geometry of salt-plume originating from a point-source, with horizontal and vertical length scales b and z respectively [Turner, 1969].

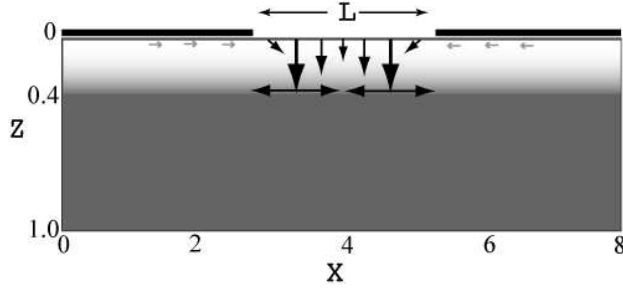


Figure 3. Schematic drawing of a 2-D lead convection in *Kozo* [1983] and *Smith IV and Morison* [1998] numerical models. Units in x-dir and z-dir are normalized. Heavy black lines at $z = 0$ represent sea-ice which can move in the x direction relative to the ocean. Typical values for mixed layer depth are $\sim 15\text{-}40\text{m}$, and for lead-width L are $\sim 50\text{-}1000\text{m}$. A halocline at depth $z = 0.4$ is qualitatively shown with the gray-scale. *Smith IV and Morison* [1998] results are qualitatively summarized here with black arrows for salt plumes and gray horizontal arrows for ocean return flows near the surface. The salt plumes first form at the lead's edges, then sink to the bottom of the mixed layer and spread horizontally (see also Plate 3 in *Smith IV and Morison* [1998]).

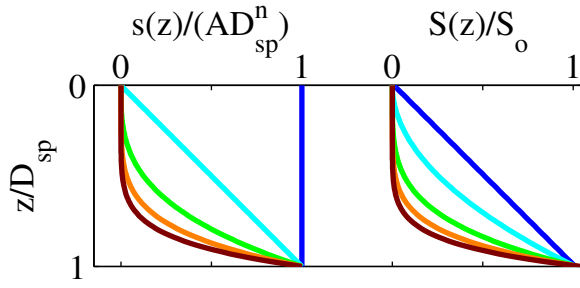


Figure 4. Normalized distribution $s(z)$ (left) and cumulative salt $S(z)$ (right) as a function of depth z and power n . Here the n values are $[0,1,3,5,7]$ with colors progressively changing from $n = 0$ in blue to $n = 7$ in dark red. *Duffy et al.* [1999] used $n = 0$ to produce a uniform distribution $s(z)$. At higher n , more salt is taken from the surface and distributed at D_{sp} . $S(z)$ is the total accumulation at depth, such that at $z = D_{sp}$, $S(z) = S_o$ where S_o is the amount of salt rejected during sea-ice formation.

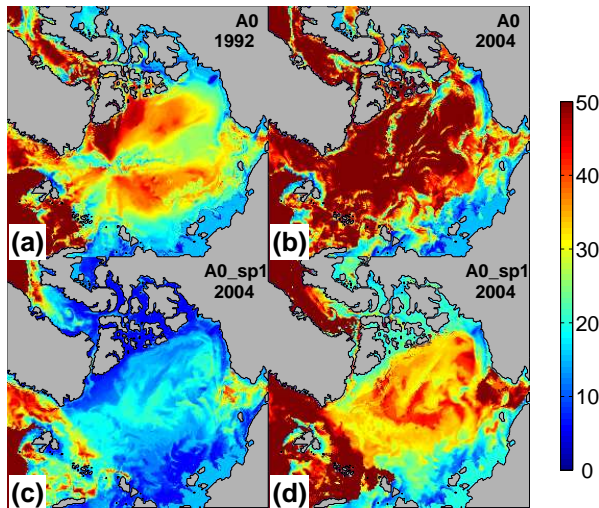


Figure 5. Monthly mixing layer depth in meters in (a) February 1992, (b) February 2004 (b) for the baseline experiment **A0**, (c) February 2004, and (d) the corresponding salt-plume depth D_{sp} for the experiment with salt-plume scheme turned on **A0.sp1**. The salt-plume depth in (d) as defined using a $d\rho/dz$ criterion mimics the mixing layer depth in (c) and is approximately 10-15m below it. Without the salt-plume scheme (b), mixed layer depth are too deep compared to observations.

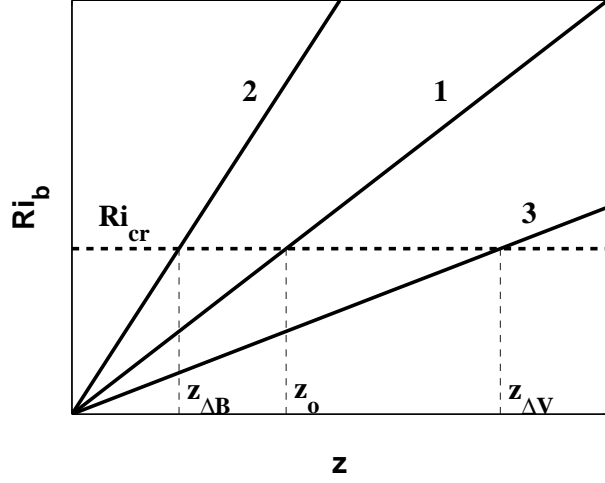


Figure 6. Schematic plot of the local bulk Richardson number Ri_b in the oceanic boundary layer, as defined in the KPP vertical mixing scheme, as a function of depth z . Curves 1-3 represent a reference case (1), a case with increased buoyancy difference between the surface and at the bottom of the mixing layer (2), and a case with increased differential shear velocities (3). For a given critical bulk Richardson number Ri_{cr} , locations z_o , $z_{\Delta B}$ and $z_{\Delta V}$ define the oceanic boundary layer depth for the three cases respectively. Values of z are relative, with $z_{\Delta B} < z_o < z_{\Delta V}$.

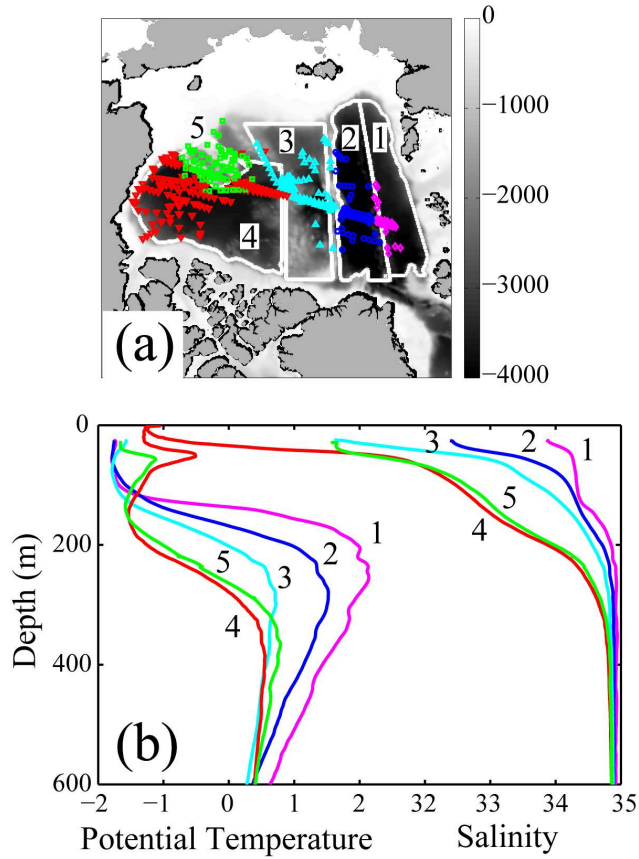


Figure 7. (a) Locations of data in the Nansen (purple, 1), Amundsen (dark blue, 2), Makarov (light blue, 3), and Canadian Basins (red, 4), and Chukchi Cap (green, 5). (b) Typical vertical temperature and salinity profiles in the basins and Chukchi Cap based on observations. Colors and numbers correspond to the basins as identified in (a). Temperature unit is degree Celsius.

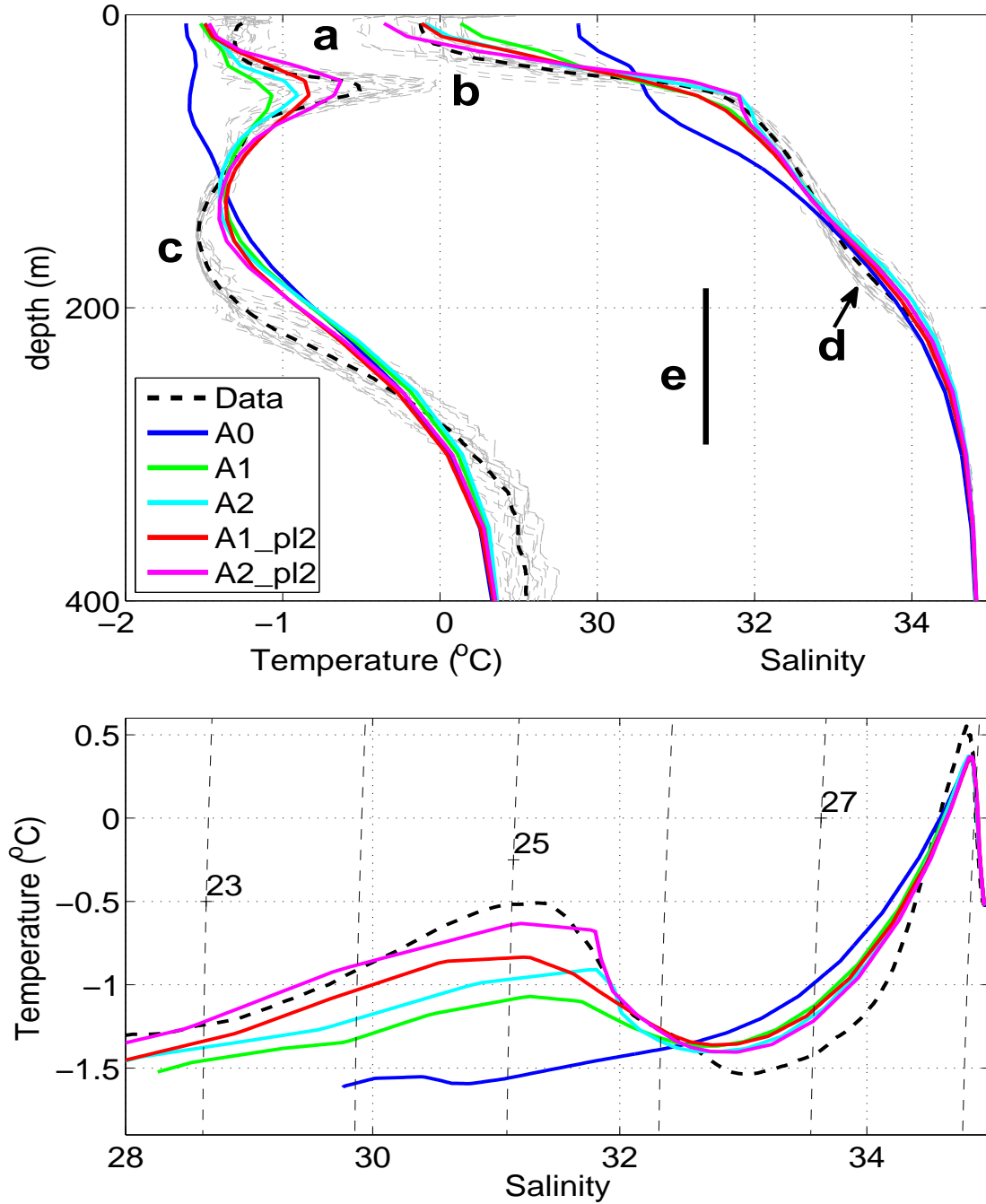


Figure 8. Vertical temperature and salinity structures (upper panel) and T/S diagram (lower panel) of the Canadian Basin in August 2003 for the experiments listed in Table 1. In the upper panel, the actual CTD measurements are shown in light gray, with the data mean shown in dashed heavy black. Additional annotations are a) mixed layer, b) summer Pacific Water source, c) winter Pacific Water source, d) salinity break indicating halocline of Pacific origin above and Atlantic origin (e, vertical bar) below [Rudels *et al.*, 2004]. Dashed contours in T/S diagram are

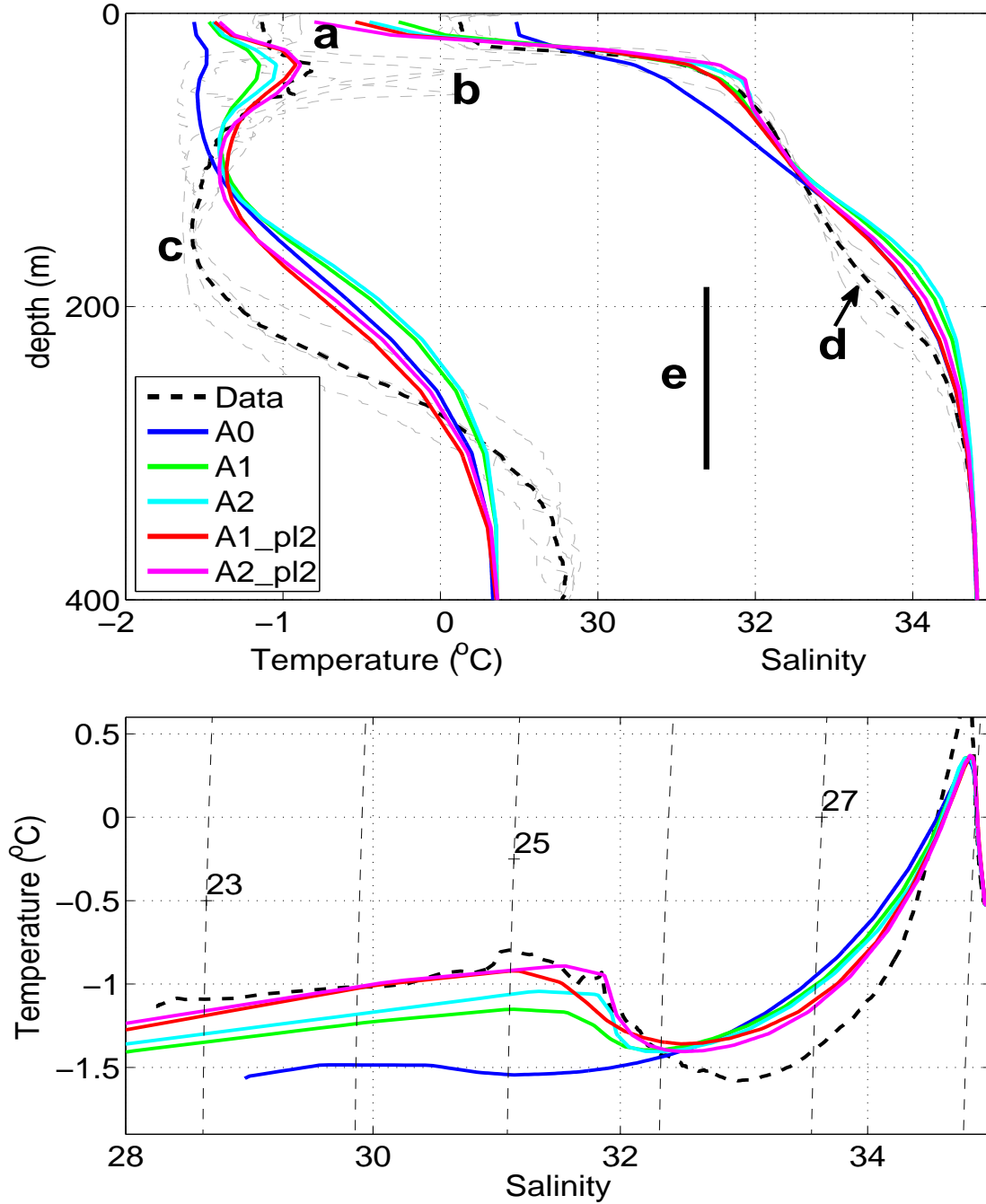


Figure 9. Vertical temperature and salinity structures and TS diagrams of the Chukchi Cap region in August 2003 for the experiments listed in Table 1. In the upper panel, the actual CTD profiles are shown in light gray, with the mean shown in dashed heavy black. Annotations a-e are the same as in Fig 8. Dashed contours in T/S diagram are density anomaly.

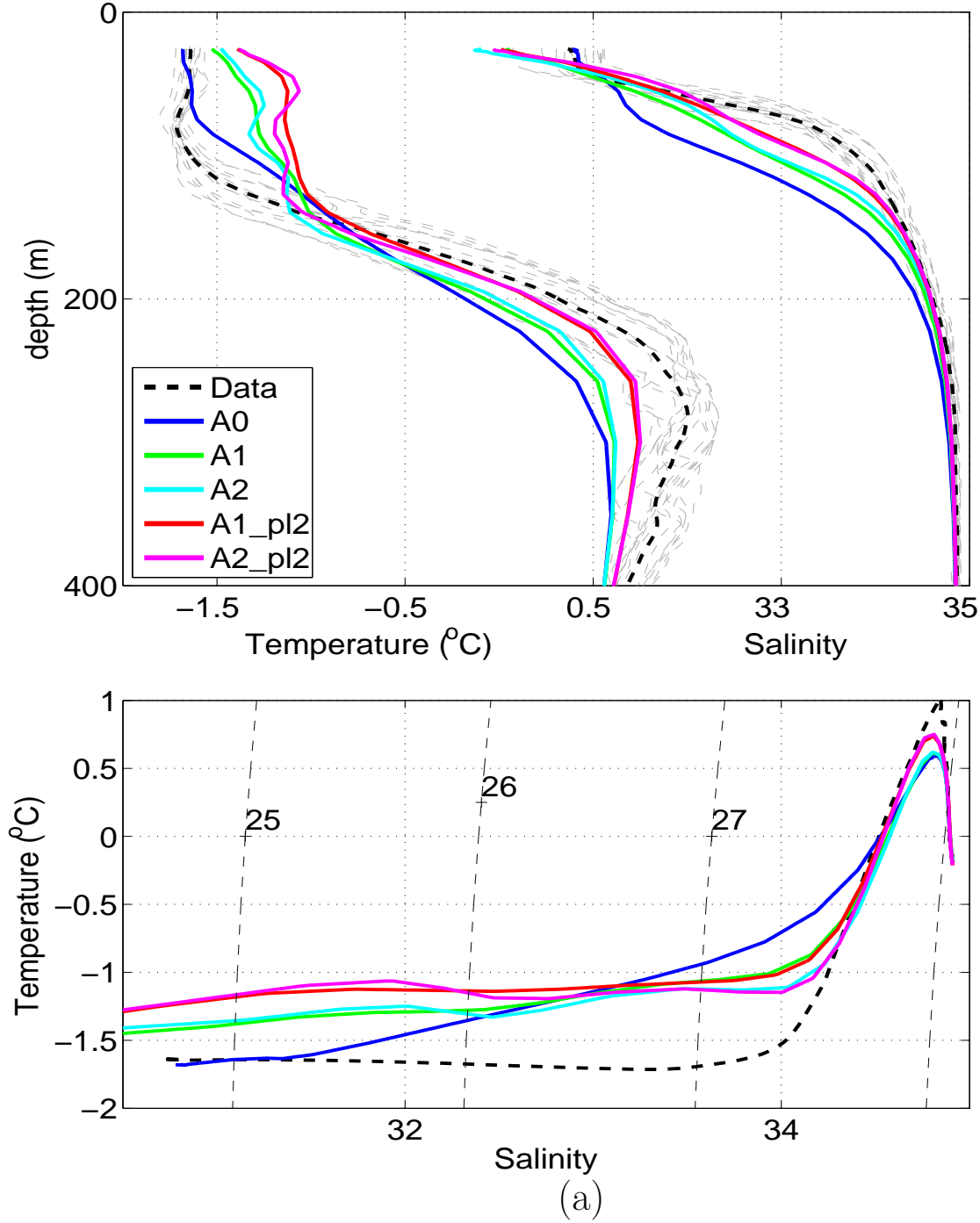


Figure 10. October 2000 vertical temperature and salinity structures in the (a) Makarov Basin and (b, opposite page) Amundsen Basin for the experiments listed in Table 1. In the upper panels, the actual CTD profiles are shown in light gray, with the mean shown in dashed heavy black. Dashed contours in T/S diagram are density anomaly.

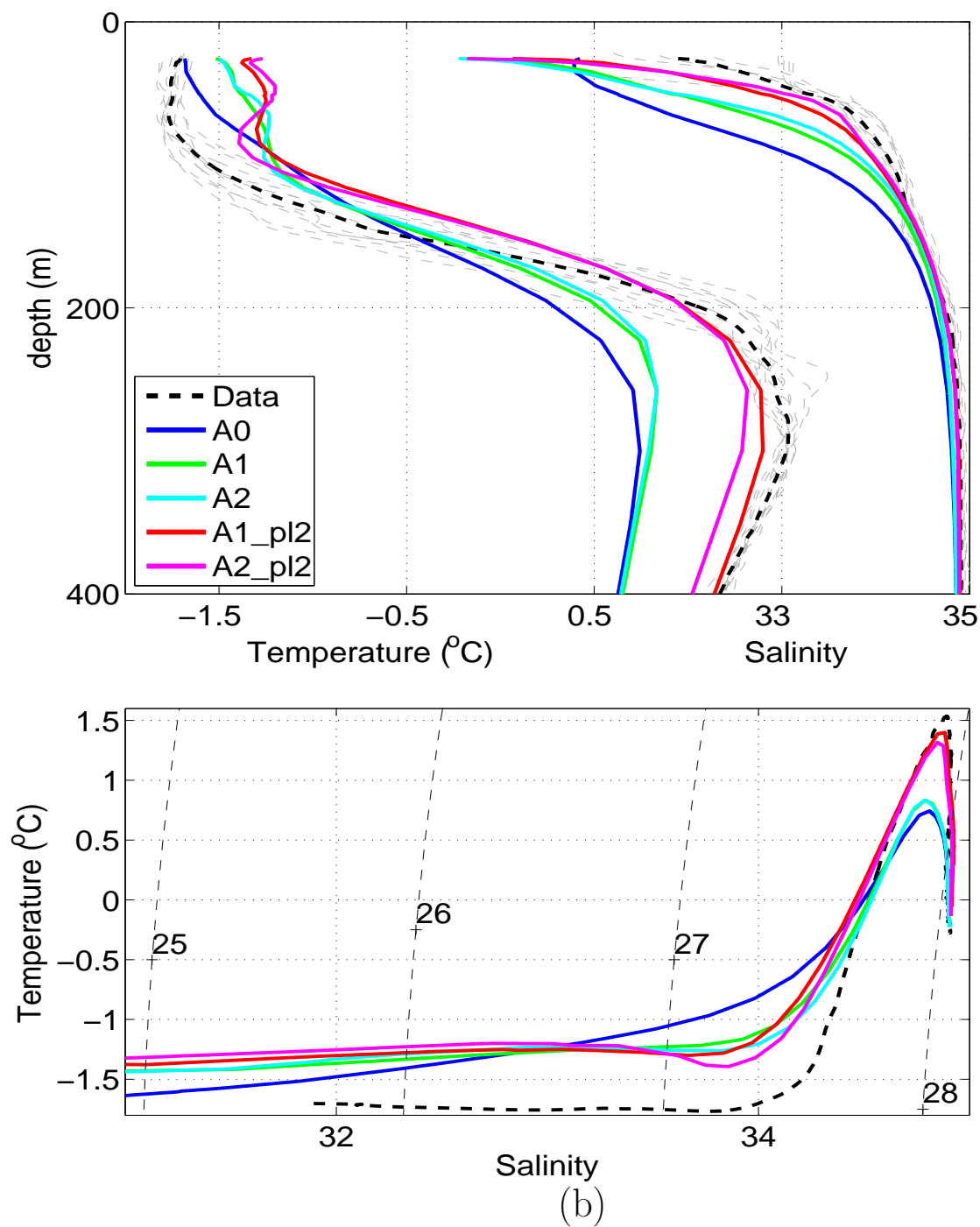


Figure 10. Cont'd.

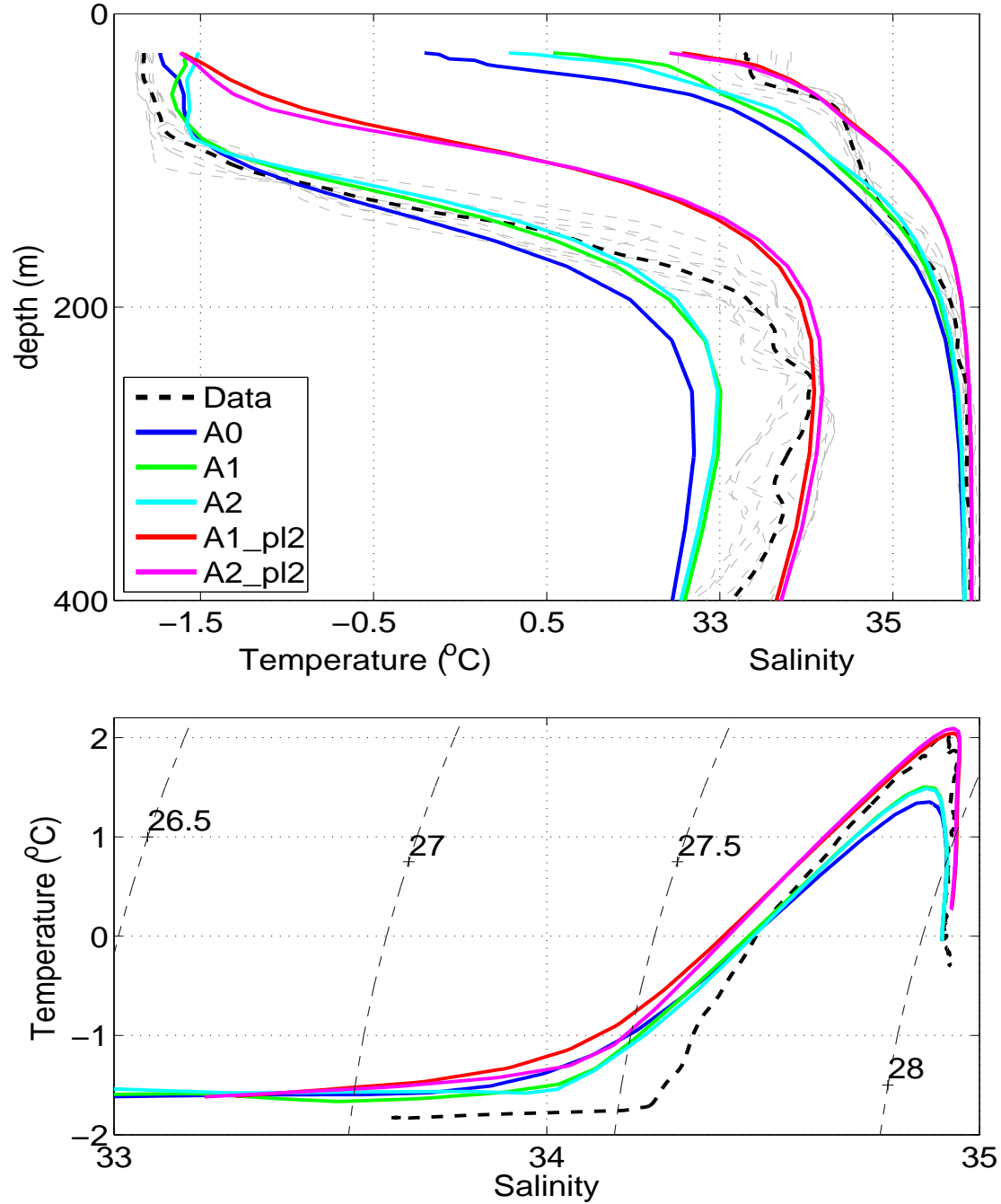


Figure 11. Vertical temperature and salinity structures in the Nansen Basin for October 2000 for the experiments listed in Table 1. In the upper panel, the actual CTD profiles are shown in light gray, with the mean shown in dashed heavy black. Dashed contours in T/S diagram are density anomaly.

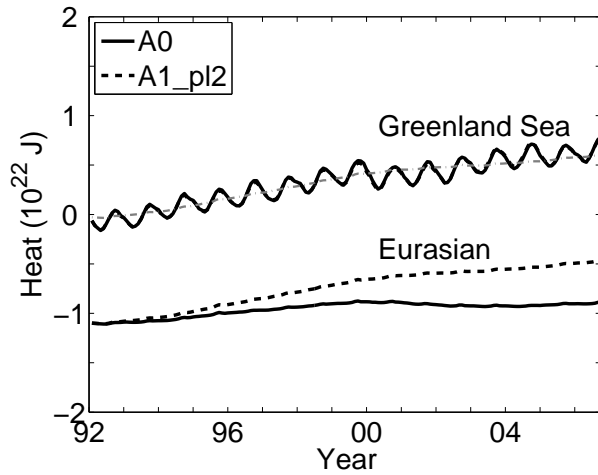


Figure 12. Total heat content in the Eurasian Basin (Nansen and Amundsen combined) and Greenland Sea for the baseline experiment **A0** (black solid line) and salt-plume experiment **A1_pl2** (black dashed line). There is no difference in the heat content between the two solutions in the Greenland Sea. The gray dash-dot line is the heat content of the Eurasian Basin for solution **A1_pl2** with a vertical offset to match heat content in the Greenland Sea. Based on the similar trends, the heat build-up in the Eurasian basin is entirely explained for by the heat trend in the Greenland Sea (compare gray dash-dot line to line for the Greenland Sea heat content).

Table 1. List of experiments

Salt_plume	^a $\nu = 10^{-5} m^2/s$	$\nu = 10^{-6} m^2/s$	$\nu = 0 m^2/s$
off	A0	A1	A2
sp1	A0_sp1	A1_sp1	A2_sp1
sp2 ^b	A0_sp2	A1_sp2	A2_sp2

^a ν is the background diffusivity used in the KPP vertical mixing scheme.

^b Perturbation experiment to distribute rejected salt to a deeper depth than in *sp1*.

Table 2. Percentage of improvements $I(\%)$

		Canadian Basin				Chukchi Cap				Makarov Basin				Amundsen Basin				Nansen Basin			
Data	Salt Plume	M ^a	$\nu(m^2/s)$			M	$\nu(m^2/s)$			M	$\nu(m^2/s)$			M	$\nu(m^2/s)$			M	$\nu(m^2/s)$		
			10 ⁻⁵	10 ⁻⁶	0		10 ⁻⁵	10 ⁻⁶	0		10 ⁻⁵	10 ⁻⁶	0		10 ⁻⁵	10 ⁻⁶	0		10 ⁻⁵	10 ⁻⁶	0
sc93 ^b	off		–	–	–		–	–	–		–	–	–		–	–	–		–	–	–
	sp1	5	–	–	–	0	–	–	–	4	–	–	–	4	–	–	–	0	–	–	–
	sp2		–	–	–		–	–	–		–	–	–		–	–	–		–	–	–
sc95	off		0 ^c	38	28		–	–	–		0	9	7		0	15	15		0	2	-1
	sp1	28	24	-1	2		–	–	–	26	3	4	2	13	127	60	55	5	-8	4	1
	sp2		27	-6	-15		–	–	–		-1	1	0		78	78	75		-23	-20	-19
sc96	off		0	47	51		0	-17	-20		0	24	27		–	–	–		–	–	–
	sp1	25	23	23	20	34	-18	-39	-36	16	17	22	25	4	–	–	–	2	–	–	–
	sp2		16	11	6		-30	-46	-50		19	29	30		–	–	–		–	–	–
sc97	off		0	64	66		–	–	–		0	21	28		–	–	–		–	–	–
	sp1	43	40	53	51	6	–	–	–	29	18	19	23	8	–	–	–	2	–	–	–
	sp2		39	47	45		–	–	–		24	29	30		–	–	–		–	–	–
sc98	off		0	19	16		0	23	20		0	57	66		0	22	-246		0	23	-10
	sp1	16	23	26	21	15	5	12	6	48	-26	26	39	15	19	46	-171	9	56	55	70
	sp2		12	37	27		-14	9	2		-52	14	28		29	60	-133		31	57	66
sc99	off		0	41	35		0	-3	-30		0	34	40		0	-5	-7		0	13	6
	sp1	31	26	38	34	16	24	14	-20	12	16	36	46	18	56	54	42	7	57	11	32
	sp2		28	39	30		6	30	4		26	46	52		54	64	59		26	-10	-9
sc00	off		0	-4	-14		–	–	–		0	61	74		0	64	68		0	104	97
	sp1	24	15	7	-4	0	–	–	–	14	50	74	76	10	110	136	145	8	59	-34	-7
	sp2		9	18	11		–	–	–		65	99	102		103	116	134		36	-164	-156
bgep03	off		0	98	107		0	35	13		–	–	–		–	–	–		–	–	–
	sp1	26	53	110	114	10	28	49	29	0	–	–	–	0	–	–	–	0	–	–	–
	sp2		62	116	118		17	48	26		–	–	–		–	–	–		–	–	–
bgep04	off		0	49	47		–	–	–		–	–	–		–	–	–		–	–	–
	sp1	28	48	64	53	0	–	–	–	0	–	–	–	0	–	–	–	0	–	–	–
	sp2		68	92	79		–	–	–		–	–	–		–	–	–		–	–	–

^a M is the number of CTD profiles available for each year.

^b sc[93-00] are SCICEX data for 1993-2000. bgep[03-04] are BGEP data for 2003-2004.

^c Values listed here are percentage of improvement $I(\%)$ in the sum of squares of residuals (Eqn 11).